JGR Oceans

RESEARCH ARTICLE
10.1029/2022JC018786

Ocean Surface Wind Estimation From Waves Based on Small GPS Buoy Observations in a Bay and the Open Ocean

Tomoya Shimura[1], **Nobuhito Mori**[1,2], **Yasuyuki Baba**[1], **and Takuya Miyashita**[1]

[1]Disaster Prevention Research Institute, Kyoto University, Kyoto, Japan, [2]School of Engineering, Swansea University, Swansea, UK

Key Points:

- Ocean surface wind is estimated from ocean surface wave spectrum information measured by a small global positioning system buoy
- Ocean surface wind is estimated from ocean surface waves for both bay and open ocean conditions
- The newly proposed method improves the accuracy of wind speed and direction estimations from ocean surface waves

Correspondence to:
T. Shimura,
shimura.tomoya.2v@kyoto-u.ac.jp

Citation:
Shimura, T., Mori, N., Baba, Y., & Miyashita, T. (2022). Ocean surface wind estimation from waves based on small GPS buoy observations in a bay and the open ocean. *Journal of Geophysical Research: Oceans*, *127*, e2022JC018786. https://doi.org/10.1029/2022JC018786

Received 21 APR 2022
Accepted 25 AUG 2022

Abstract Ocean surface wind and wave information is important in a wide variety of areas, such as coastal disaster reduction, offshore structure design, and atmosphere-ocean flux estimation. This study proposed a new method for ocean surface wind estimation from surface wave spectrum information measured by small global positioning system buoys. The concept of this method relies on the assumption that the high-frequency part of the ocean-wave spectrum is proportional to $u_* f^{-4}$ where u_* is the friction velocity and f is the frequency. The determination algorithm for the coefficient of f^{-4} was optimized in this study. The wind direction was determined by the wave cross-spectrum, assuming that the wind direction aligns the propagation direction of the high-frequency part of the wave. The proposed wind estimation method was applied to bay and open ocean observations, and the performance of the proposed wind estimation method was similar between the bay and the open ocean. The proposed method improves the wind estimation especially in coastal areas and at high wind speeds in the open ocean compared with the previous method. The performance of the method of the previous study differs between the bay and open ocean due to their spectral shape differences. High-quality wind and wave information can be obtained using the proposed method. If the mass deployment of small drifting buoys covered the global ocean, the information based on the proposed method could be considerably powerful, and could compensate for the weakness of satellite-based wind and wave estimations.

Plain Language Summary Ocean observations are spatially sparse compared with on-land observations because of the difficulty of observation platform development. However, ocean wind and wave information is important in a wide variety of areas, such as coastal disaster mitigation and offshore structure design. Recently, readily deployed small global positioning system (GPS)-tracked buoys for wave observation have been developed that have the potential to fill gaps in observations through mass deployment. This study proposes a new ocean wind speed and direction estimation method using ocean wave information derived from a small GPS buoy. The performance of the proposed method was validated and compared with data of the observed wind. It was shown that the proposed method can be applied to any type of wave condition, whereas the applicability of the previous method was limited. The proposed method allows for high-quality ocean wind and wave information to be simultaneously collected.

1. Introduction

Winds over the ocean generate surface waves, which are among the main factors causing coastal disasters (Tamura et al., 2021), beach morphology changes (Kuriyama et al., 2012), ship routing decisions (Padhy et al., 2008), and offshore structure design (Chen et al., 2014). Therefore, ocean surface wave forecasting, hindcasting, reanalysis, and future projections are important in these areas. Numerical models of ocean waves are driven by ocean surface wind data, and their accuracy depends mainly on the quality of that data. Ocean surface winds are also important in their own right. Recently, offshore wind power generation has become increasingly efficient for sustainable development (Jansen et al., 2020), and offshore wind estimation is critical for this production. Furthermore, ocean surface winds determine air-sea fluxes, such as momentum flux, heat flux, and gas flux (Cronin et al., 2019). Momentum flux is one of the main factors in tropical cyclone development (Emanuel, 1988). Global heat flux in the context of climate change can control the balance between atmospheric temperature increase and ocean heat content (and the resultant rise in global sea-level; Roemmich et al., 2015). Air-sea flux of greenhouse gases, such as CO_2 can affect the acceleration of global warming (Sarmiento et al., 1998). Air-sea flux also depends on wave conditions (Shimura et al., 2017, 2020, 2022).

Despite the importance of wind and wave information as described above, observations of ocean surface winds and waves have been limited spatially and temporally due to the difficulty of establishing an observation platform in the ocean. Currently, the main available data are collected from moored buoys. The US National Oceanic and Atmospheric Administration's National Data Buoy Center (NDBC) provides observed wind and wave data from a moored buoy network (https://www.ndbc.noaa.gov/), although the spatial coverage of the ocean is limited. In addition to direct observation, remotely sensed satellites can provide indirect estimations. Sea surface wind speed has been estimated using satellite radiometers (e.g., Ebuchi, 2017), altimeters (e.g., Ribal & Young, 2019), scatterometers (e.g., Spencer et al., 2000), and synthetic aperture radar (e.g., Horstmann et al., 2003). Sea surface roughness, which is caused by sea surface wind, is represented by the brightness temperature in radiometers and the normalized radar cross-section in altimeters, scatterometers, and synthetic aperture radar. The information on sea surface roughness is converted to wind speed using geophysical model functions. The weaknesses of satellite-based wind estimation include high wind-speed conditions, rain contamination, and spatial resolution (Bourassa et al., 2019). Although wave heights can be estimated by satellite altimeters (Ribal & Young, 2019), detailed wave information (wave spectra) cannot be estimated by satellites. Swell (long period) wave spectra have been provided by Sentinel-1/SAR (Hasselmann et al., 2013) and spectra with directional ambiguity have been generated by the recently launched CFOSAT/SWIM radar (Hauser et al., 2020); however, satellite-retrieved wave information is limited compared with that from direct observation.

A small, easy-to-deploy, global positioning system (GPS) wave buoy has recently been developed (Raghukumar et al., 2019), and has the potential to fill the gap of sparse ocean wave observation by mass deployment in the global ocean (Ardhuin et al., 2019; The Washington Post, 2020). The buoy measures the wave spectra and bulk wave parameters. The wave buoy is small for easy deployment, and thus, it is difficult to install anemometers onto the buoy, unlike the NDBC buoys. On the other hand, ocean wave spectra are related with wind friction velocity. Toba (1973) and Phillips (1985) found that the high-frequency part of the ocean wave spectrum is proportional to $u_* f^{-4}$ where u_* is the friction velocity and f is the wave frequency. This means that the friction velocity can be estimated using the high-frequency energy of the ocean waves, and converted to wind speed based on the wind profile. Thomson et al. (2013) and Voermans et al. (2020) demonstrated the validity of ocean surface wind estimation based on the relationship with ocean wave spectra in the high-frequency range measured by ocean wave buoys. Jiang (2022) established a deep neural network for the estimation of sea surface wind from wave spectra, although the relationship between high-frequency ocean wave spectra and wind was not explicitly used. A small GPS wave buoy, Spotter (Houghton et al., 2021), incorporates a wind estimation function based on the methods of Thomson et al. (2013) and Voermans et al. (2020). This study improved the wind estimation from ocean wave spectra using Spotter. We demonstrated the validity of the proposed wind estimation method under both bay and open ocean conditions. Collocated ocean wave and wind data are useful. Buoy observations cannot be interrupted by rain and can capture local wind, which is a weakness of remotely sensed satellite-based wind estimations.

2. Methodology

2.1. Small GPS Buoy

The "Spotter" buoy developed by Sofar Ocean was used for ocean surface wave observations (Raghukumar et al., 2019; https://www.sofarocean.com/products/spotter-smart-mooring-by-sofar). Spotter is 42 cm in diameter, 31 cm in height, and weighs 5.3 kg (7.4 kg including the ballast chain). The natural frequency is 1.2 Hz (Raghukumar et al., 2019). Spotters have been increasingly used for ocean surface wave observations worldwide (Kodaira et al., 2021; Lancaster et al., 2021; Smit et al., 2021). Spotter utilizes GPS-based ocean-wave measurements (Joodaki et al., 2013). The three-dimensional displacement of the buoy was measured by GPS at a 2.5 Hz sampling rate. Wave statistics were calculated using the displacement data. The bulk wave parameters (significant wave height, peak wave period, mean wave period, peak wave direction, and mean wave direction), variance density spectrum, directional moments, and geographical coordinates (longitude and latitude) were transmitted through satellite communication. The three-dimensional displacement data were stored on an onboard SD card. This study used the spectral power density of the vertical displacement and the cross-spectral power density between the vertical and horizontal displacements for sea-surface wind estimation. The spectral power density was calculated using the 2.5 Hz displacement data stored in the SD card of Spotter.

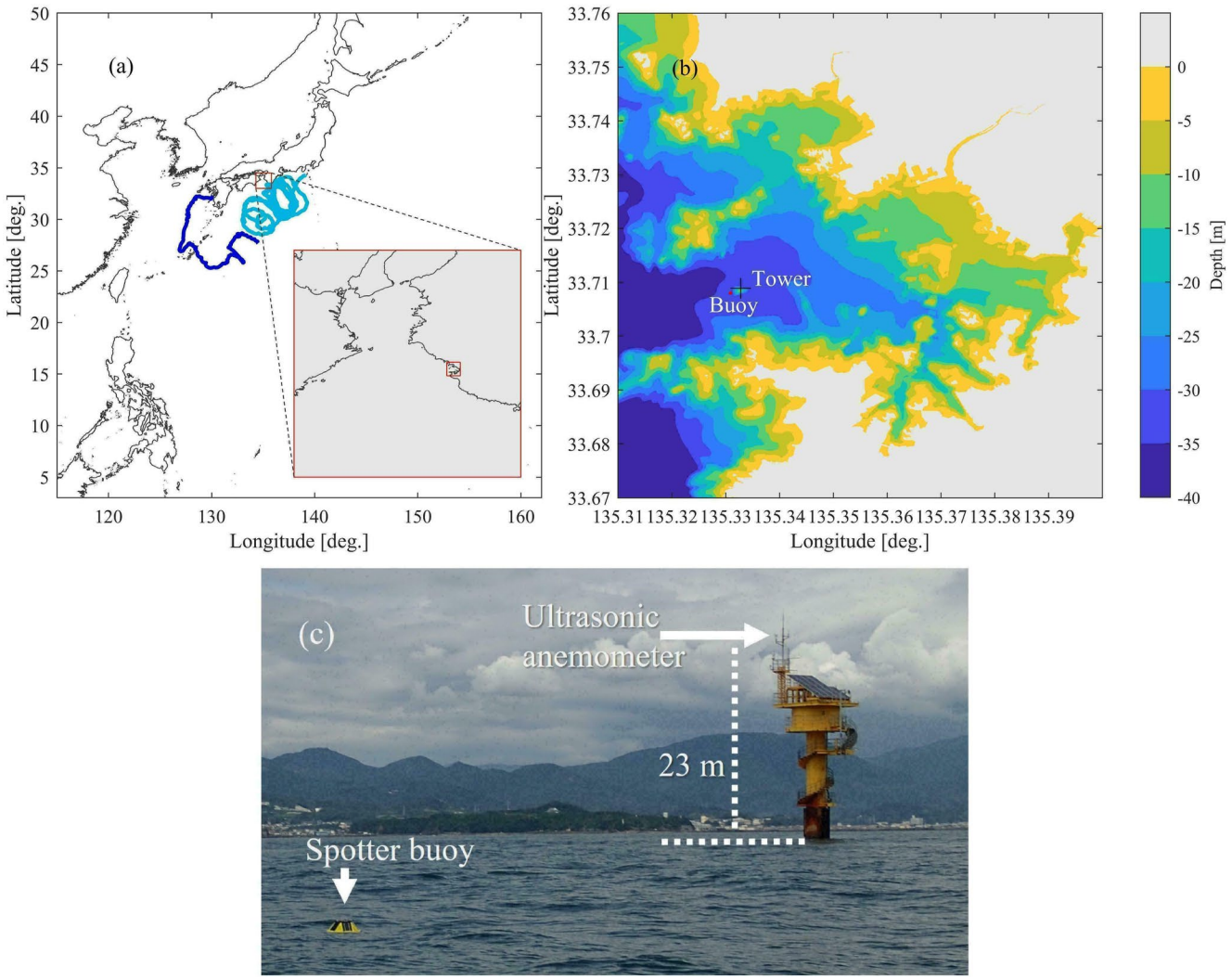

Figure 1. The observation locations. Panel (a) and (b) show the location of Tanabe bay in Japan. Panel (b) is a magnified map of the red-lined box area in the gray-shaded area of panel (a). The location of the observation tower and the moored buoy are shown by the black cross and red dot, respectively, in panel (b). Panel (c) shows the snapshot of the moored buoy and the observation tower. The two colored lines in panel (a) show the paths of the two drifting buoys for open ocean observations.

2.2. Observations in the Bay

Ocean surface wave observations were conducted by mooring Spotter at the mouth of Tanabe Bay, Wakayama, Japan (Figure 1). Tanabe Bay is open to the west and has a bay mouth approximately 4 km long (Figure 1b). The water depth around the bay mouth is approximately 30 m, and the Disaster Prevention Research Institute at Kyoto University has an observation tower (Figure 1c) on a 10 m depth mound at the bay mouth (33°42′32″N and 135°19′58″E; Figure 1b). Meteorological and oceanographic observations have been conducted operationally for wind, solar radiation, atmospheric temperature, humidity, pressure, ocean surface waves, and water temperature. The wind speed and direction data measured at a height of 23 m from the sea surface using an ultrasonic anemometer and waves measured by a radio-wave meter were used in this study.

Spotter was moored near the observation tower (Figures 1b and 1c), and the observations were conducted during the summers of 2020 and 2021. The period of observation in 2020 was from 17 July to 12 October, and that in 2021 was from 8 July to 10 October. Spotter was moored at about 200 m from the tower and moved within an 80 m diameter circle from 135.3308°E to 135.3316°E in longitude and from 33.7077°N to 33.7083°N in latitude during the 2020 observation period, and from 135.3304°E to 135.3316°E in longitude and from 33.7077°N to 33.7084°N during the 2021 observation period. The wind and wave conditions measured by the observation

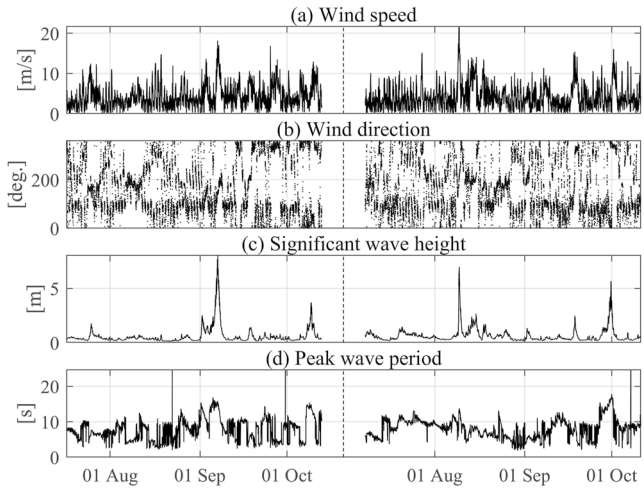

Figure 2. Wind and wave conditions during the bay observation. (a) Wind speed at 23 m height from sea surface, (b) wind direction, (c) significant wave height, and (d) peak wave period. The observed values were derived from tower measurements. Left and right parts indicate the observation in 2020 and 2021, respectively.

tower during the observation periods in 2020 and 2021 are shown in Figure 2. The wind data consisted of 30 min averaged data, and the wave data were derived from 30 min length data. The maximum wind speeds in 2020 and 2021 were 18.1 and 21.7 m/s, respectively. The maximum significant wave heights in 2020 and 2021 were 8.0 and 7.0 m, respectively. These severe conditions were induced by typhoons. Although winds came from every direction, east winds predominated (60–120-degree wind direction covered 33% of all observations).

The validity of the wave measurements by Spotter is demonstrated here. Figure 3a shows a comparison of the significant wave heights between Spotter and the tower observations. The color indicates the peak wave period, as measured by Spotter. Regarding the shorter wave period, the comparison shows agreement between the tower and Spotter's observations. When the peak wave period is less than 15 s, the correlation coefficient, root mean square error (RMSE), and bias are 0.98, 0.17, and −0.02 m. Wave heights determined by Spotter underestimated those of the tower when the wave periods were long. When the peak wave period is more than 15 s, the correlation coefficient, RMSE, and bias are 0.96, 0.92, and −0.64 m. This was due to wave shoaling. The mooring location for Spotter was 30 m in depth and close to the tower, but the tower is located on a 10 m depth mound (Figure 1b). The wave shoaling was simply considered using linear wave theory. The measured significant wave heights (H), peak wave numbers (k), and depth (h), were used to derive the offshore wave heights (H_0) as $H/H_0 = [\tanh kh(1 + 2kh/\sinh 2kh)]^{-1/2}$. Figure 3b shows a comparison of the estimated offshore wave heights observed by the tower and Spotter. The comparison indicates a better agreement, although Spotter still underestimated the high waves. When the peak wave period is more than 15 s, the correlation coefficient, RMSE, and bias are 0.97, 0.42, and −0.15 m. The underestimation can be attributed to the simple shoaling estimation described above, or possibly wave focusing on a mound (or due to the bottom bathymetry).

2.3. Observations in the Open Ocean

The characteristics of waves and wind can differ between a bay and the open ocean. Open ocean observations were conducted by drifting Spotters. Two Spotters were drifted into the southern ocean of Japan in the summer of 2021. One was released on 29 May (JST) from Shinsei-maru of the Japan Agency for Marine-Earth Science and Technology (JAMSTEC; sailing number KS-21-9) and reached the coast on 26 October. The other was released on 6 June from Ryofu-maru of the Japan Meteorological Agency (JMA; RF21-05) and reached the coast on 24 August. The drifting paths are shown in Figure 1a. Figure 4 presents the significant wave heights observed by the two drifted Spotters. The Spotters experienced several severe wave conditions, with significant wave heights of more than 5 m. Severe conditions occurred because of typhoon waves. The 9 m significant wave heights observed by SPOT-1270 were caused by a typhoon (Typhoon No. 202106, IN-FA). Significant wave heights of more than 7 m were observed by SPOT-1269, which resulted from two typhoons (No. 202109, Lupit and 202116, MINDULLE).

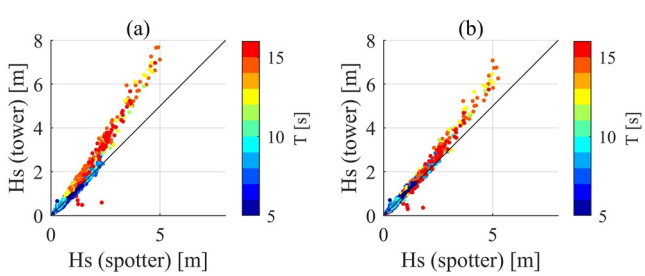

Figure 3. The comparison of significant wave heights between Spotter and the tower observations. (a) Significant wave heights and (b) converted offshore wave heights. The colors indicate the peak wave period from Spotter's measurements.

2.4. Method for Ocean Surface Wind Estimation From a Wave Spectrum

The method for ocean surface wind estimation is based on information from the wave spectral tail. The wave spectrum was calculated using 2.5 Hz displacement data measured by the Spotters. Prior to the spectral analysis, the 2.5 Hz displacement data were filtered using the fourth order high pass Butterworth filter. The passband was set to 0.027 Hz. The spectral analysis was conducted using the Welch method with a Hamming window of 102.4 s

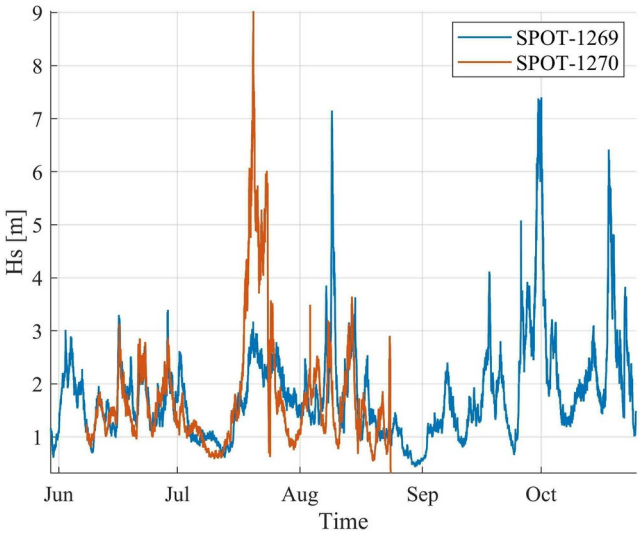

Figure 4. The significant wave heights observed by the two drifting Spotters in the open ocean in 2021. The drifting paths are shown in Figure 1a.

length with 50% overlap. The following wave spectral quantities were used in the proposed method.

$E_{zz}(f)$: Surface elevation variance density spectrum (unit: m^2s)
$A_{zx}(f)$: Amplitude spectrum of z-x cross spectrum (unit: m^2s)
$A_{zy}(f)$: Amplitude spectrum of z-y cross spectrum (unit: m^2s)
$\Phi_{zx}(f)$: Phase spectrum of z-x cross-spectrum (unit: radian)
$\Phi_{zy}(f)$: Phase spectrum of z-y cross-spectrum (unit: radian)

where f is the frequency, and z, x, and y are the vertical, east-west, and north-south coordinates, respectively. The cross-spectrum S_{zx} and S_{zy} can be written as:

$$S_{zx}(f) = A_{zx}(f)e^{i\Phi_{zx}(f)} \tag{1}$$

$$S_{zy}(f) = A_{zy}(f)e^{i\Phi_{zy}(f)} \tag{2}$$

The basic concept of wind speed estimation is based on the analytic expression of the wave energy spectrum in the wind-wave equilibrium range proposed by Phillips (1985). The energy spectrum can be represented by the f^{-4} shape of the spectral tail (Phillips, 1985; Toba, 1973) and the energy level of the equilibrium range (E_0) is represented as:

$$E_{zz}(f) = \frac{4\beta I u_* g}{(2\pi)^3} f^{-4} = E_0 f^{-4} \tag{3}$$

where β is a constant, I is the directional spreading function, u_* is the frictional velocity, and g is the gravitational acceleration (Thomson et al., 2013; Voermans et al., 2020). The wind profile $U(z)$ can be represented by the law of the wall, as follows:

$$U(z) == \frac{u_*}{\kappa}\ln\left(\frac{z}{z_0}\right) \tag{4}$$

where z is the height from the sea surface, κ is the von Kalman constant, and z_0 is the roughness length. The roughness length can be represented by the Charnock relationship (Charnock, 1955),

$$z_0 = 0.11\frac{\upsilon}{u_*} + \alpha\frac{u_*^2}{g} \tag{5}$$

where υ is the air dynamic viscosity coefficient, and α is the Charnock coefficient. Based on Equations 3–5, theoretical ocean surface wind profile $U(z)$ can be determined when the energy level of the equilibrium range E_0 is derived from the wave spectrum and the given parameters β, I, α. Parameter I depends on wave directionality (Phillips, 1985), and it was set to 2.5, which is a common value, as indicated by Thomson et al. (2013). The Charnock coefficient α was set to 0.018, which is a typical value (Hersbach, 2011). Although the Charnock parameter can vary by the wave conditions (Fairall et al., 2003), a constant value was used in this study. The parameter β was optimized by minimizing RMSE between the estimated and measured wind speeds. As a result, parameter β was determined to be 0.016, within the range of Juszko et al. (1995).

The derivation of the equilibrium range and E_0 from a given wave spectrum is the core of surface wind-speed estimation. Thomson et al. (2013) determined the equilibrium range as the 20 neighboring frequency bands with the best fit to f^{-4}, which is typically 0.2–0.4 Hz (0.15–0.35 Hz under very high wind speeds). The method of Voermans et al. (2020) also finds the range with the best fit to the f^{-4} shape, and data that did not fit the f^{-4} shape with a certain criterion were excluded from the analysis. Spotter has an onboard function to estimate wind speed (Houghton et al., 2021) with the method of finding the equilibrium range with the best fit to f^{-4} similar to that of Thomson et al. (2013) and Voermans et al. (2020). Hereafter, this method is referred to as the best-fit method. However, the method proposed in this study does not find the range with the best fit to the f^{-4} shape. E_0 is derived as follows:

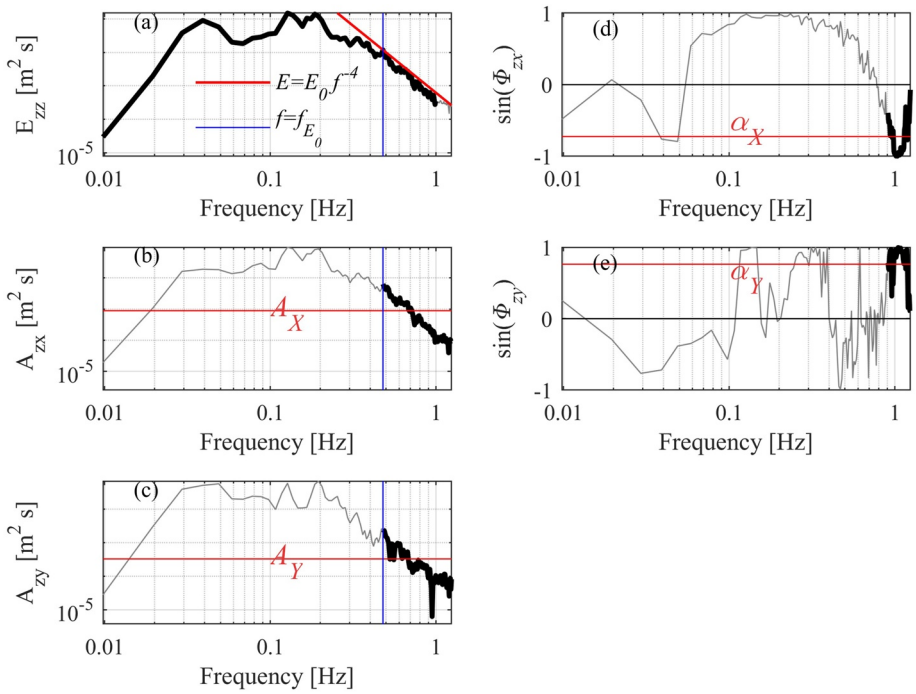

Figure 5. An example of ocean surface wind estimation from a wave spectrum by the Max-E0 method. (a) Estimation of E_0 for wind speed estimation, (b–e) estimation of A_X, A_y, α_X, α_Y for wind direction estimation. The thin gray lines in the panels are the raw spectra, and the thick lines are the spectra within the frequency range used for the wind speed and direction estimation: $0 \le f \le f_{\max\_zz}$ for the surface elevation variance density spectrum, $f_{E_0} \le f \le f_{\max\_xy}$ for the amplitude spectrum, and $f_{\min\_xy} \le f \le f_{\max\_xy}$ for the phase spectrum. E_o, f_{E_0}, A_X, A_Y, α_X, and α_Y in Equations 6–12 are depicted using red and blue lines.

$$E_0 = \max_{0 \le f \le f_{\max\_zz}} E_{zz}(f) f^4 = E_{zz}\left(f_{E_0}\right) f_{E_0}^4 \tag{6}$$

Equation 6 indicates that E_0 is defined as the maximum value of $E_{zz}(f)f^4$ and the frequency of the maximum value is denoted as f_{E_0}. Finding the range with the best fit to f^{-4} shape requires several criteria of fitness. However, the method based on Equation 6 can determine E_0 clearly and easily. This method is referred to as the Max-E0 method. The $f_{\max\_zz}$ in Equation 6 was set to 1 Hz, although a frequency of up to 1.24 Hz is available. This is because $f_{\max\_zz} = 1$ Hz provides a better estimation than 1.24 Hz. An example of this method is shown in Figure 5a. It is clear that the estimated $E_o f^{-4}$ is well-fitted to the spectral tail shape.

The wind direction is determined by the wave cross-spectrum, assuming that the wind direction aligns with the propagation direction of the high-frequency part of the wave. Spectral quantities $A_{zx}(f)$, $A_{zy}(f)$, $\Phi_{zx}(f)$, and $\Phi_{zx}(f)$ were used for the estimation. The wind direction D (direction the wind came from) was estimated as follows:

$$\theta_1 = \tan^{-1}\left(\frac{\int_{f_{E_0}}^{f_{\max\_xy}} A_{zx}(f)\mathrm{d}f}{\int_{f_{E_0}}^{f_{\max\_xy}} A_{zy}(f)\mathrm{d}f}\right) = \tan^{-1}\left(\frac{A_X \times \left(f_{\max\_xy} - f_{E_0}\right)}{A_Y \times \left(f_{\max\_xy} - f_{E_0}\right)}\right) \tag{7}$$

$$\theta_2 = C_{\text{enhance}}\left(\theta_1 - \frac{\pi}{4}\right) + \frac{\pi}{4} \tag{8}$$

$$\theta_3 = \begin{cases} \theta_2, 0 \le \theta_2 \le \dfrac{\pi}{2} \\ 0, \quad \theta_2 < 0 \\ \dfrac{\pi}{2}, \quad \theta_2 > \dfrac{\pi}{2} \end{cases} \tag{9}$$

$$\alpha_X = \frac{1}{(f_{\max\_xy} - f_{\min\_xy})} \int_{f_{\min\_xy}}^{f_{\max\_xy}} \sin\left(\Phi_{zx}(f)\right) \mathrm{d}f \tag{10}$$

$$\alpha_Y = \frac{1}{(f_{\max\_xy} - f_{\min\_xy})} \int_{f_{\min\_xy}}^{f_{\max\_xy}} \sin\left(\Phi_{zy}(f)\right) \mathrm{d}f \tag{11}$$

$$D = \begin{cases} \theta_3 + \pi, & \alpha_X \le 0 \text{ and } \alpha_Y \le 0 \\ -\theta_3 + 2\pi, & \alpha_X \le 0 \text{ and } \alpha_Y > 0 \\ -\theta_3 + \pi, & \alpha_X > 0 \text{ and } \alpha_Y \le 0 \\ \theta_3, & \alpha_X > 0 \text{ and } \alpha_Y > 0 \end{cases} \tag{12}$$

Here, $f_{\max\_xy}$ was set to 1.24 Hz and $f_{\min\_xy}$ was set to 0.9 Hz based on trial and error. The wind direction was estimated using Equation 7, which is the ratio of the tail of the amplitude spectrum of the *z*-*x* and *z*-*y* cross spectra (Kuik et al., 1988). θ_1 was not close to zero or $\pi/2$. Therefore, the range of θ_1 is widened by factor C_{enhance} in Equation 8. Here, C_{enhance} was set to 1.2 by trial and error. θ_1 ranged from 0 to $\pi/2$. The quadrant of the wind direction is determined by Equations 10–12 using the phase spectrum. An example of the application of this method is shown in Figures 5b–5e.

3. Results

The accuracy of the proposed wind speed and direction estimation method (Max-E0 method) is demonstrated. This method was applied to observations in Tanabe Bay. First, the estimated E_0 using Equation 6 was compared with the measured wind speed. Figure 6a shows a comparison of the estimated E_0 and the tower wind speed. All data (7,589 units) were used for this comparison, except for missing data. The E_0 had a good correlation with the measured wind speed. The correlation coefficient was 0.83, which indicates the validity of the relationship between the wave spectrum and wind speed (Equation 3).

The estimated E_0 was converted to wind speed using Equations 3–5. The results of the comparison between the estimated (Max-E0 method) and measured wind speeds are shown in Figure 6b. The comparison reveals a good agreement. The correlation coefficient, bias, and RMSE were 0.83, −0.03 s, and 1.48 m/s, respectively. The bias was small (−0.03 m/s) on average. However, the high wind speed tended to be underestimated by Spotter. The maximum wind speeds estimated by Spotter and the observation were 16 and 20 m/s, respectively. This can be attributed to the constant Charnock parameter. Varying the Charnock parameter with wind and wave conditions can improve the estimation. This is left for future research. Overall, we can conclude that the wind speed estimation (Max-E0 method) was accurate. The constant parameters β and I can also cause an underestimation of the high wind speed.

The results of the wind direction estimation (Max-E0 method) are shown in Figure 6c. The circular correlation coefficient (Fisher & Lee, 1983), bias, and RMSE were 0.84, 7, and 39°, respectively. Therefore, the proposed Max-E0 method can capture the sea-surface wind direction. The gap was observed at a wind direction of approximately 270°. The wind directions just below 270° were underestimated and those just above 270 were overestimated. Although this could be due to the fault of the proposed method or tower distortion effects on the measured winds, the clear reason for this gap was not identified in this study. The wind direction was estimated by assuming that the wind direction aligned to the propagation direction of the high-frequency part of the wave. The propagation direction of the high-frequency part of the wave can also be considered to align to the wind stress direction. Previous studies have shown that wind and wind stress directions can be misaligned depending on swell wave conditions (Chen et al., 2020; Potter et al., 2015). Therefore, a deviation of the estimated wind direction from the observation can be caused by swell impacts on the wind stress direction to some extent.

Spotter also has an onboard function to estimate wind speed using the best-fit method (Houghton et al., 2021; Thomson et al., 2013; Voermans et al., 2020). The results of the best-fit method are presented. The estimated wind data were derived from Spotter's onboard function and were not independently derived from the wave spec-

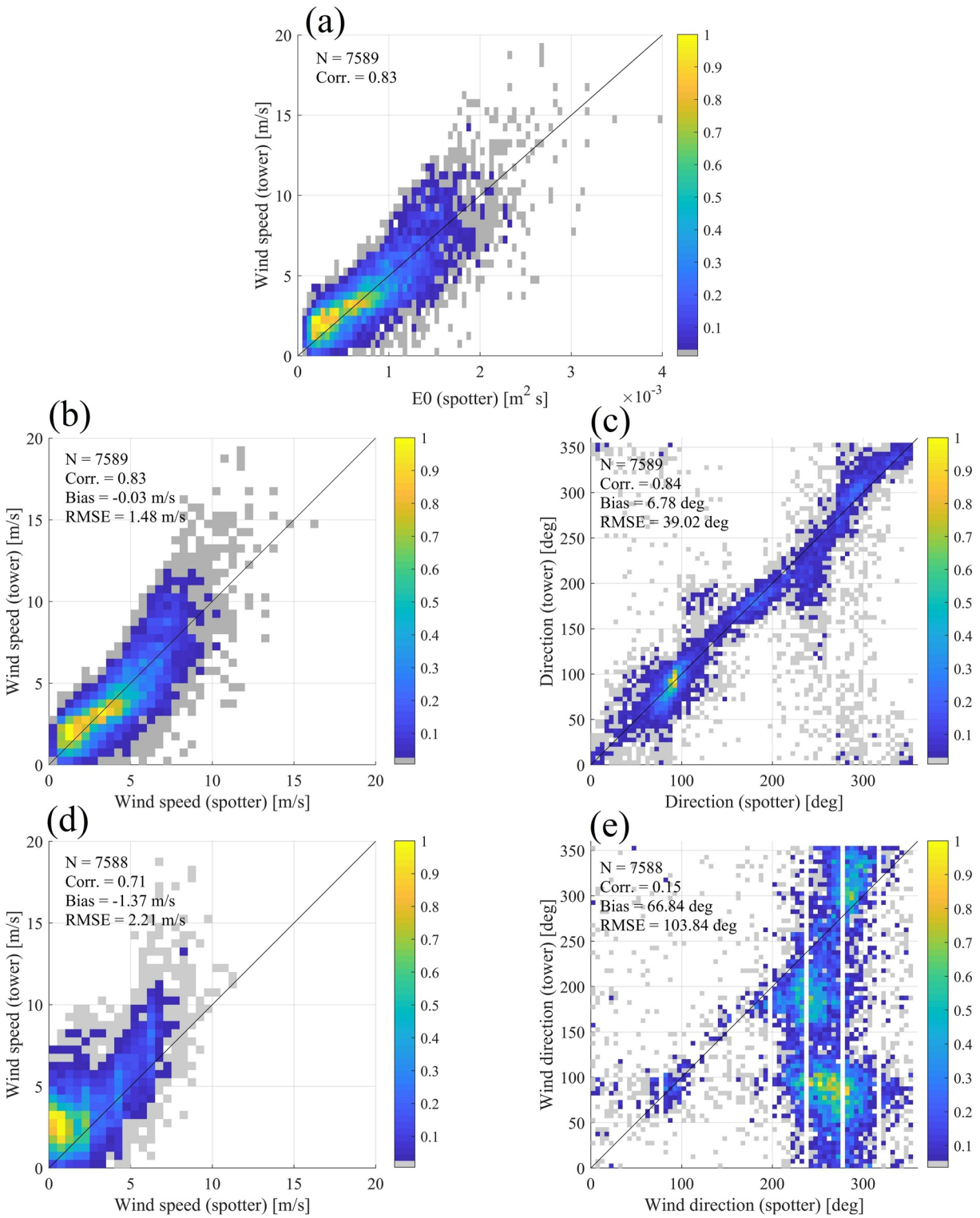

Figure 6. The comparison of wind speed and direction estimated from wave spectra in the bay with the wind measured by the tower. (a) The comparison of estimated E_0 with measured wind speed. (b) The comparison of estimated wind speed by Max-E0 method with the measured wind speed. (c) The comparison of estimated wind direction by Max-E0 method with the measured wind direction. (d, e) are same as (b, c) using the estimation by the best-fit method. The colors indicate data density normalized by the maximum data density.

tra ourselves. Spotter's onboard function estimates wind at 10 m height from sea surface. Therefore, the measured wind speed at 23 m height was converted to that at 10 m height based on Equations 4 and 5. A comparison of wind speed and direction between the estimation by the best-fit method and tower observation is shown in Figures 6d and 6e. For wind speed, the correlation coefficient, bias, and RMSE were 0.71, −1.37, and 2.21 m/s, respectively. Although the correlation was relatively high, the wind speed was underestimated, particularly high wind speeds. It was probably difficult to generate wind speeds greater than 10 m/s from the best-fit method because the waves are not fully developed in this environment (fetch and duration limited condition). The best-fit method failed to estimate the wind direction. Therefore, the proposed Max-E0 method significantly improved the estimation of wind speed and direction under wind and wave conditions in the bay.

Next, observations of the open ocean are presented. Wind speed at a height of 10 m above the sea surface and wind direction were estimated using the Max-E0 method, similar to the bay observations. Since there is no direct observation in the open ocean, the estimated wind was compared with atmospheric reanalysis data. Wind speeds and directions at the 10 m height were obtained from ERA-5 reanalysis (Hersbach et al., 2020). Figures 7a and 7b show the results of the comparison of wind speed and direction between the estimation from the wave spectra by the proposed Max-E0 method and the ERA-5 reanalysis. Both the wind speed and direction showed strong agreement between the estimation and reanalysis. The correlation coefficient, bias (from ERA-5), and root mean square difference (RMSD) were 0.85, 0.10, and 1.84 m/s, respectively. Regarding the wind direction, the correlation coefficient, bias (from ERA-5), and RMSD were 0.84, −4°, and 35°, respectively. These values are consistent with the results of the comparison between the estimated and observed values in the bay (Figure 6). Although this reanalysis does not necessarily reflect reality, we can conclude that the proposed Max-E0 method can provide good wind estimations in the open ocean. Figures 7c and 7d show the results of onboard wind estimation (best-fit method). The correlation coefficients of wind speed and direction are 0.76 and 0.83, which are similar to those in the study of Houghton et al. (2021). The wind estimated by best-fit method underestimates the high wind speed. On the other hand, Max-E0 shows better agreement for high wind speed. Although the Max-E0 method shows improved agreement with the reanalysis over the best-fit method, the latter can provide better estimations for the open ocean than those for the bay. The performances of the Max-E0 and best-fit method are summarized in Table 1.

4. Discussion

The performance of wind estimation by the best-fit method (onboard function) was different between the bay and open ocean. The difference is discussed in terms of the spectral shape characteristics. The normalized frequency (f^*) and normalized spectrum (E^*_{zz}) are defined as $f^* = f/f_{E_0}$ and $E^*_{zz}(f^*) = E_{zz}(f^*)/E_{zz}\left(f_{E_0}\right)$. Figure 8 shows the normalized spectra observed in the bay (panel a) and the open ocean (panel b). All data are represented in the figure by thin gray lines. The averaged spectra are indicated by thick black lines. The averaged spectrum in the bay is also shown in panel b as a thick gray line. The average values were calculated using $\log_{10} E^*_{zz}$. The color contour indicates the data density. For both the data in the bay and the open ocean, the spectral shape higher than the f_{E_0} is well represented by f^{-4}. In the frequency range lower than the f_{E_0}, the result in the open ocean shows a denser data range with f^{-4} shape than that in the bay. This means that the spectra in the open ocean tend to have a longer f^{-4} shaped tail than those in the bay. In fact, the averaged f_{E_0} in the bay observation was 0.67 Hz and that in the open ocean was 0.38 Hz. Some spectra in the open ocean show the steeper tails than those in the bay. It can be considered that tails of some spectra in the open ocean can show transition from equilibrium range (f^{-4}) to saturation range (f^{-5}) (Lenain & Melville, 2017; Phillips, 1985) because of the longer available tail length in the open ocean. In addition, the spectra of the bay tended to have several peaks. Therefore, the data-dense range at a lower frequency in the bay observation showed a constant E^*_{zz} value of 1–2. In contrast, in the open ocean, E^*_{zz} clearly increases with increasing in frequency at lower frequencies. Overall, the spectral shape in the open ocean tended to have a clear f^{-4} shaped tail and a smaller number of peaks. Therefore, the method of identifying the frequency range with the best fit to the f^{-4} shape (best-fit method) could easily find the range because of the clear spectral shape in open ocean observations. However, the best-fit method failed to find the range in the bay observation due to the complicated spectral shape. In contrast, the proposed Max-E0 method can estimate wind well under both bay and open ocean conditions.

Figure 9 shows the frequency distributions of the estimated wind speeds in the bay and open ocean. The Max-E0 method underestimated the high wind speed in the bay compared with the observations. Regarding the open

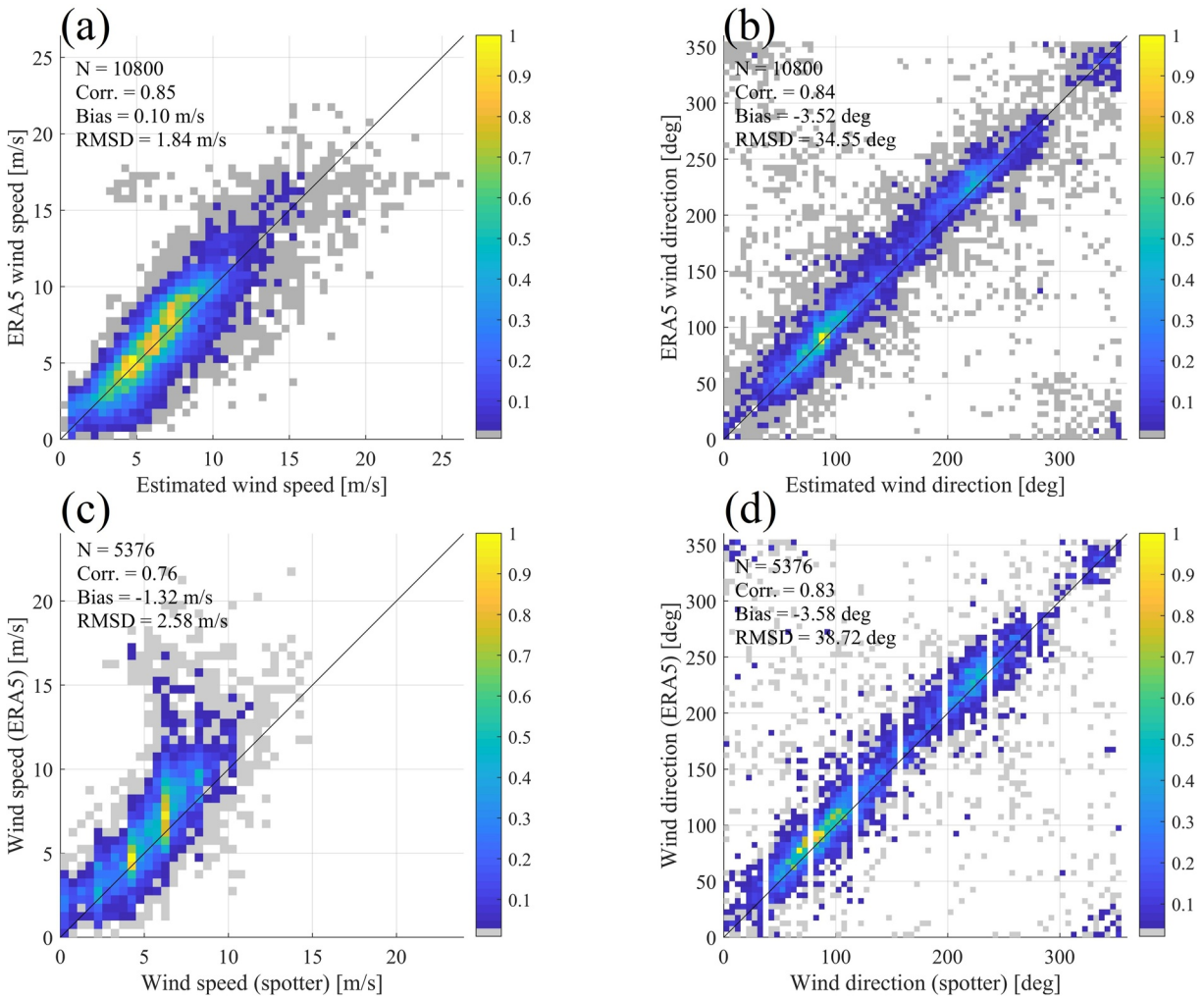

Figure 7. The comparison of wind speed and direction estimated from wave spectra in the open ocean with the reanalysis ERA-5. (a) The comparison of estimated wind speed by Max-E0 with ERA-5. (c) The comparison of estimated wind direction by Max-E0 with ERA-5. (c, d) are same as (a, b) using the estimation by the best-fit method. The color indicates the data density and the data density is normalized by the maximum value.

ocean, the Max-E0 method agreed well with the ERA-5 reanalysis. The ERA-5 represented the winds with a scale of several tens of kilometers. Therefore, it can be speculated that higher wind speeds occurred locally than those of the ERA-5, and the Max-E0 method underestimated these higher wind speeds. Thus, the accuracy of high wind speed estimation should be improved. In this study, parameters β, I, and α were set as constant values.

Table 1
Summarized Performance of Max-E0 and Best-Fit Wind Estimation Method

	Bay (reference is observation)			Open ocean (reference is ERA5)		
	Corr. coef.	RMSE	Bias	Corr. coef.	RMSE	Bias
Speed						
Max-E0	0.83	1.48 m/s	−0.03 m/s	0.85	1.84 m/s	0.10 m/s
Best-fit	0.71	2.21 m/s	−1.37 m/s	0.76	2.58 m/s	−1.32 m/s
Direction						
Max-E0	0.84	39°	7°	0.84	35°	−4°
Best-fit	0.15	104°	67°	0.83	39°	−4°

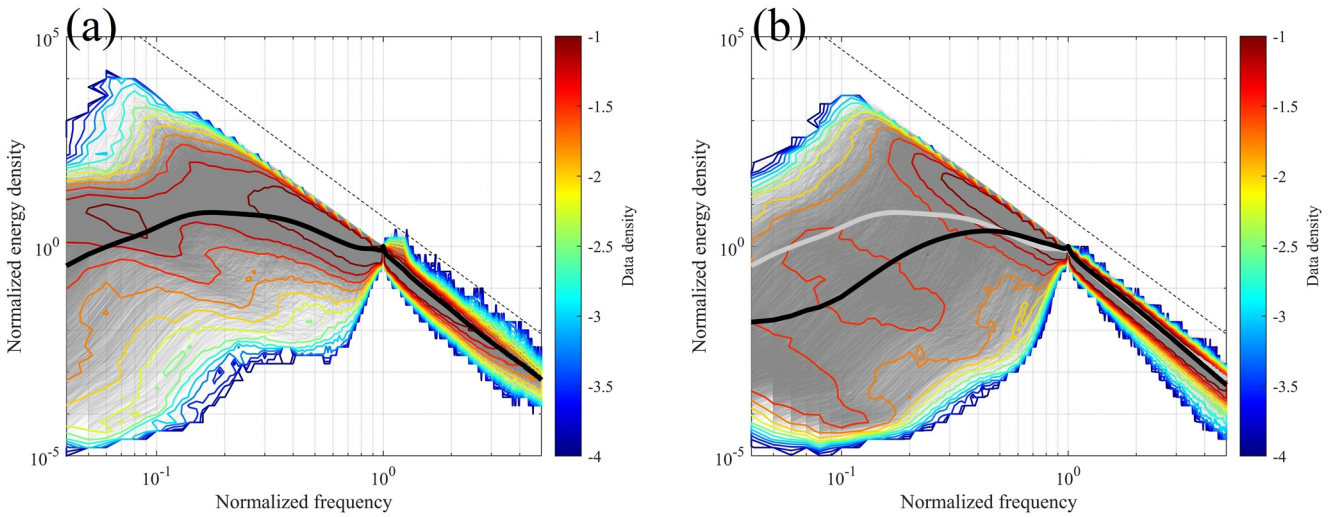

Figure 8. The normalized wave spectra in the bay (a) and open ocean (b). All data are shown as thin gray lines. The averaged spectra are indicated by thick black lines. The averaged spectrum in the bay is also shown in panel (b) as a thick gray line. The color contours indicate the data density represented by $\log_{10}N$, where N is the normalized data density by the maximum value. The broken line is the line of f^{-4}.

The variations in β, I, and α depending on the wind and wave conditions proved promising for improved accuracy. Furthermore, the applicability of the proposed method to more extreme wind speed, for example, higher than 30 m/s, has not been confirmed yet. Powell et al. (2003) shows that the behavior of air-sea momentum transfer under extreme wind conditions (more than 30 m/s) is different than moderate wind; drag coefficient is not increased for the range of wind speed more than 30 m/s. Therefore, the applicability should be investigated in the future work.

This study has chosen the frequencies of f_{max_zz}, f_{min_xy}, and f_{max_xy} as 1, 0.9, and 1.24 Hz, respectively. The sensitivity of estimated wind to the frequencies is shown in Figure 10. The correlation coefficient, RMSE, and bias between estimated wind and tower-observed wind, are shown changing the frequencies of f_{max_zz}, f_{min_xy}, and f_{max_xy}. Note that parameters β, I, and α are not changed. Regarding the estimated wind speed (Figures 10a–10c), the performance is not varied much where f_{max_zz} is beyond 0.8 Hz (RMSE ranges 1.47–1.63 m/s). The sensitivity of estimate wind direction to f_{min_xy} and f_{max_xy} are shown where f_{max_zz} is fixed to 1 Hz (Figures 10d–10f). The performance doesn't depend on f_{max_xy} and is not varied much where f_{min_zz} is 0.8–1.1 Hz (RMSE ranges

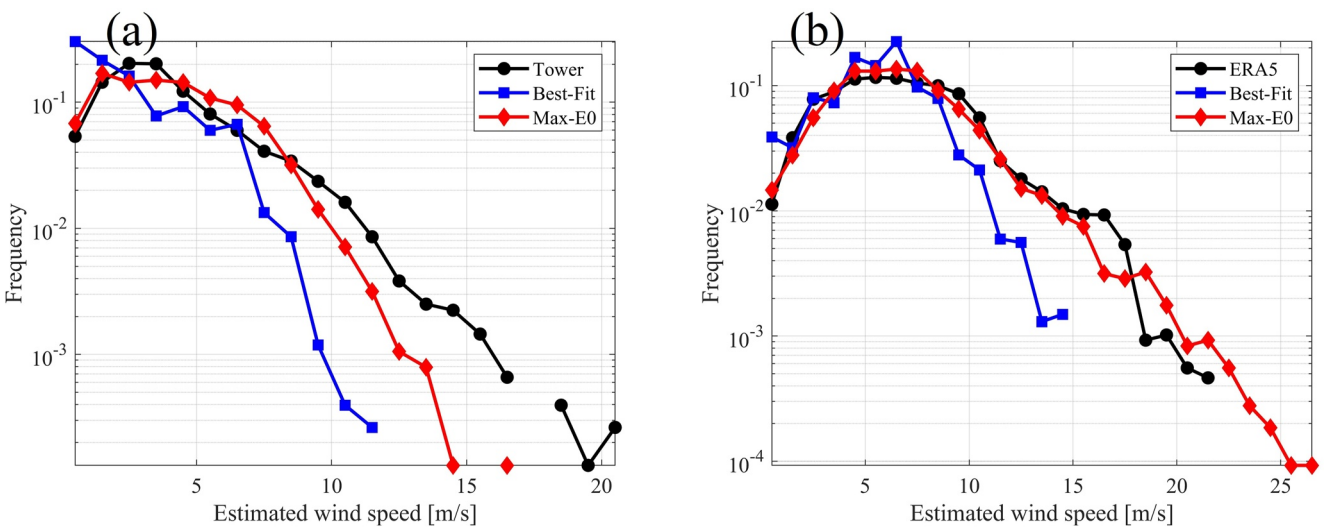

Figure 9. The frequency distributions of estimated wind speeds in the bay (a) and open ocean (b).

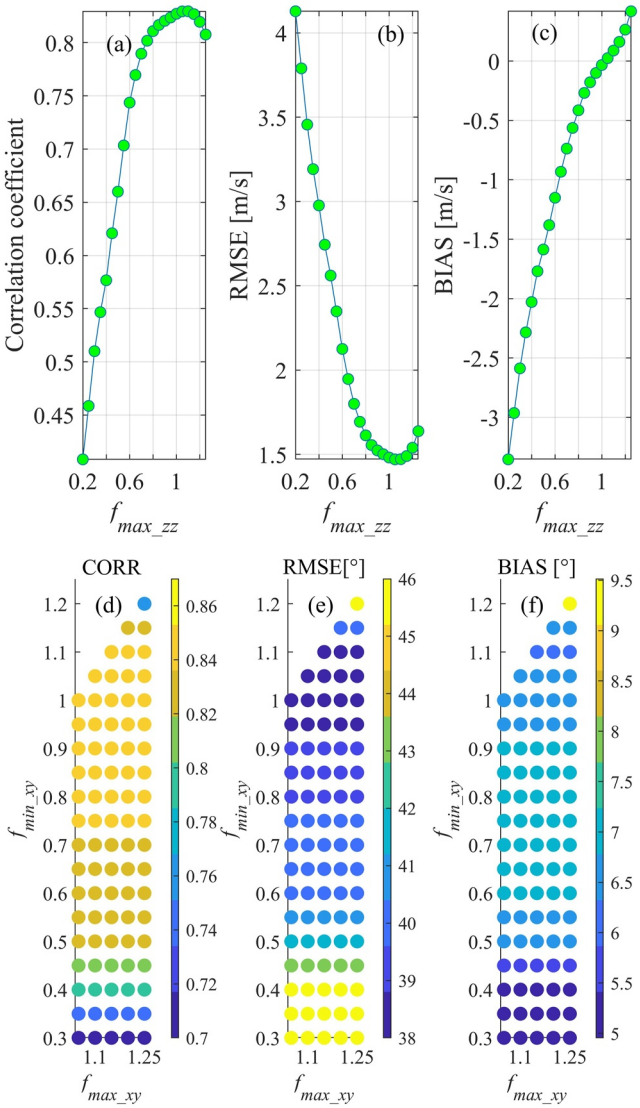

Figure 10. The sensitivity of Max-E0 method to the frequency parameters. Upper panels show the sensitivity of estimated wind speed to f_{max_zz} represented by (a) correlation coefficient, (b) root mean square error (RMSE), (c) bias against tower observation. Lower panels show the sensitivity of estimated wind direction to f_{min_xy} and f_{max_xy} represented by (d) correlation coefficient, (b) RMSE, (c) bias.

38–39°). The wave spectra in this study were estimated by the Welch method reducing noise as described in the Section 2.4. If raw spectra derived from the Fourier Transform are used, the Max-E0 method can produce different results because the raw spectra have large uncertainty in energy density at any given frequency. The spectra must be robust to apply the Max-E0 method.

5. Conclusions

Ocean surface wind and wave information is important for coastal disaster mitigation, beach morphology changes, ship routing decisions, offshore structure design, and atmosphere-ocean flux estimation. This study proposed a new method for ocean surface wind estimation from ocean surface wave spectrum information measured by small GPS buoys. The concept of this method relies on the fact that the high-frequency part of the ocean-wave spectrum is proportional to $u_* f^{-4}$. If the coefficient of f^{-4} can be determined from the ocean wave spectrum, the friction velocity u_* can be calculated and converted to wind speed using a given wind profile. In the proposed method, the coefficient (E_0) is simply determined as $E_o = \max E_{zz}(f) f^4$ where $E_{zz}(f)$ is the measured surface elevation variance density spectrum. The wind direction is also determined by the wave cross-spectrum, assuming that the wind direction aligns with the propagation direction in the high-frequency part of the wave.

The proposed estimation method was applied to ocean wave observations using a small GPS buoy (Spotter) in the bay and comparing with tower-observatory wind measurements. The results showed a strong agreement between the estimation and tower measurements. Regarding wind speed, the correlation coefficient, bias, and RMSE were 0.83, −0.03, and 1.48 m/s, respectively. Regarding wind direction, the circular correlation coefficient, bias, and RMSE were 0.84, 7°, and 39°, respectively. This is superior to Spotter's original function estimation based on previous studies (Houghton et al., 2021; Thomson et al., 2013; Voermans et al., 2020). Furthermore, the proposed estimation method was applied to open ocean observations. This estimation agreed well with the reanalysis data (ERA-5). Therefore, the performance of the proposed wind estimation method did not differ between the bay and the open ocean. However, the performance of the method in the previous study was different. This is due to the spectral shape differences between the bay and the open ocean.

High-quality wind and wave information was obtained using the proposed method. If the mass deployment of small drifting buoys covered the global ocean, the information based on the proposed method would be significantly powerful, compensating for the weakness of satellite-based wind and wave estimations. We expect that this method will be improved. This study used the law of wall and the Charnock relation with a constant Charnock coefficient to convert friction velocity to wind speed. The relationship between friction velocity and wind speed can depend on wave conditions. Therefore, the incorporation of wave effects into the wind estimation method is left for future studies.

Data Availability Statement

The data observed in this study are available from the ZENODO repository (https://doi.org/10.5281/zenodo.6451223).

Acknowledgments
This research was supported by JSPS KAKENHI (22K14329, 19H00782) and JST FOREST Program (JPMJFR205R). We thank Mr. Teruhiro Kubo from Kyoto University for the support in buoy deployment in Tanabe Bay, Prof. Eitaro Oka, and Dr. Hatsumi Nishikawa from the University of Tokyo for their support in buoy deployment by Shinsei-maru (KS-21-9), and Mr. Kan Ogawa and Mr. Sho Shimamura from the Japan Meteorological Agency for their support in buoy deployment by Rhofu-maru (RF21-05). We appreciate the Sofar Ocean, which provided valuable information on the Spotter buoy.

References

Ardhuin, F., Stopa, J. E., Chapron, B., Collard, F., Husson, R., Jensen, R. E., et al. (2019). Observing sea states. *Frontiers in Marine Science*, *6*(April), 1–29. https://doi.org/10.3389/fmars.2019.00124

Bourassa, M. A., Meissner, T., Cerovecki, I., Chang, P. S., Dong, X., De Chiara, G., et al. (2019). Remotely sensed winds and wind stresses for marine forecasting and ocean modeling. *Frontiers in Marine Science*, *6*(July). https://doi.org/10.3389/fmars.2019.00443

Charnock, H. (1955). Wind stress on a water surface. *Quarterly Journal of the Royal Meteorological Society*, *81*(350), 639–640. https://doi.org/10.1002/qj.49708135027

Chen, L. F., Zang, J., Hillis, A. J., Morgan, G. C., & Plummer, A. R. (2014). Numerical investigation of wave–structure interaction using OpenFOAM. *Ocean Engineering*, *88*, 91–109. https://doi.org/10.1016/j.oceaneng.2014.06.003

Chen, S., Qiao, F., Xue, Y., Chen, S., & Ma, H. (2020). Directional characteristic of wind stress vector under swell-dominated conditions. *Journal of Geophysical Research: Oceans*, *125*(7), e2020JC016352. https://doi.org/10.1029/2020JC016352

Cronin, M. F., Gentemann, C. L., Edson, J., Ueki, I., Bourassa, M., Brown, S., et al. (2019). Air-sea fluxes with a focus on heat and momentum. *Frontiers in Marine Science*, *6*(July), 430. https://doi.org/10.3389/fmars.2019.00430

Ebuchi, N. (2017). Evaluation of marine surface wind speed observations from AMSR2 on GCOM-W satellite. *IEEE Journal of Selected Topics in Applied Earth Observations and Remote Sensing*, *10*(9), 3955–3962. https://doi.org/10.1109/JSTARS.2017.2685432

Emanuel, K. A. (1988). The maximum intensity of hurricanes. *Journal of the Atmospheric Sciences*, *45*(7), 1143–1155. https://doi.org/10.1175/1520-0469(1988)045<1143:TMIOH>2.0.CO;2

Fairall, C. W., Bradley, E. F., Hare, J. E., Grachev, a. a., & Edson, J. B. (2003). Bulk parameterization of air-sea fluxes: Updates and verification for the COARE algorithm. *Journal of Climate*, *16*(4), 571–591. https://doi.org/10.1175/1520-0442(2003)016<0571:BPOASF>2.0.CO;2

Fisher, N. I., & Lee, A. J. (1983). A correlation coefficient for circular data. *Biometrika*, *70*(2), 327–332. https://doi.org/10.1093/biomet/70.2.327

Hasselmann, K., Chapron, B., Aouf, L., Ardhuin, F., Collard, F., Engen, G., et al. (2013). The ERS SAR wave mode: A breakthrough in global ocean wave observations.

Hauser, D., Tourain, C., Hermozo, L., Alraddawi, D., Aouf, L., Chapron, B., et al. (2020). New observations from the SWIM radar onboard CFOSAT: Instrument validation and ocean wave measurement assessment. *IEEE Transactions on Geoscience and Remote Sensing*, *59*(1), 5–26. https://doi.org/10.1109/TGRS.2020.2994372

Hersbach, H. (2011). Sea surface roughness and drag coefficient as functions of neutral wind speed. *Journal of Physical Oceanography*, *41*(1), 247–251. https://doi.org/10.1175/2010JPO4567.1

Hersbach, H., Bell, B., Berrisford, P., Hirahara, S., Horanyi, A., Munoz-Sabater, J., et al. (2020). The ERA5 global reanalysis. *Quarterly Journal of the Royal Meteorological Society*, *146*(730), 1999–2049. https://doi.org/10.1002/qj.3803

Horstmann, J., Schiller, H., Schulz-Stellenfleth, J., & Lehner, S. (2003). Global wind speed retrieval from SAR. *IEEE Transactions on Geoscience and Remote Sensing*, *41*(10), 2277–2286. https://doi.org/10.1109/TGRS.2003.814658

Houghton, I. A., Smit, P. B., Clark, D., Dunning, C., Fisher, A., Nidzieko, N. J., et al. (2021). Performance statistics of a real-time Pacific Ocean weather sensor network. *Journal of Atmospheric and Oceanic Technology*, *38*(5), 1047–1058. https://doi.org/10.1175/JTECH-D-20-0187.1

Jansen, M., Staffell, I., Kitzing, L., Quoilin, S., Wiggelinkhuizen, E., Bulder, B., et al. (2020). Offshore wind competitiveness in mature markets without subsidy. *Nature Energy*, *5*(8), 614–622. https://doi.org/10.1038/s41560-020-0661-2

Jiang, H. (2022). Wind speed and direction estimation from wave spectra using deep learning. *Atmospheric Measurement Techniques*, *15*(1), 1–9. https://doi.org/10.5194/amt-15-1-2022

Joodaki, G., Nahavandchi, H., & Cheng, K. (2013). Ocean wave measurement using GPS buoys. *Journal of Geodetic Science*, *3*(3), 163–172. https://doi.org/10.2478/jogs-2013-0023

Juszko, B. A., Marsden, R. F., & Waddell, S. R. (1995). Wind stress from wave slopes using Phillips equilibrium theory. *Journal of Physical Oceanography*, *25*(2), 185–203. https://doi.org/10.1175/1520-0485(1995)025<0185:WSFWSU>2.0.CO;2

Kodaira, T., Waseda, T., Nose, T., Sato, K., Inoue, J., Voermans, J., & Babanin, A. (2021). Observation of on-ice wind waves under grease ice in the western Arctic Ocean. *Polar Science*, *27*(August 2020), 100567. https://doi.org/10.1016/j.polar.2020.100567

Kuik, A. J., Van Vledder, G. P., & Holthuijsen, L. H. (1988). A method for the routine analysis of pitch-and-roll buoy wave data. *Journal of Physical Oceanography*, *18*(7), 1020–1034. https://doi.org/10.1175/1520-0485(1988)018<1020:AMFTRA>2.0.CO;2

Kuriyama, Y., Banno, M., & Suzuki, T. (2012). Linkages among interannual variations of shoreline, wave and climate at Hasaki, Japan. *Geophysical Research Letters*, *39*(6), 6604. https://doi.org/10.1029/2011GL050704

Lancaster, O., Cossu, R., Boulay, S., Hunter, S., & Baldock, T. E. (2021). Comparative wave measurements at a wave energy site with a recently developed low-cost wave buoy (Spotter), ADCP, and pressure loggers. *Journal of Atmospheric and Oceanic Technology*, *38*(5), 1019–1033. https://doi.org/10.1175/JTECH-D-20-0168.1

Lenain, L., & Melville, W. K. (2017). Measurements of the directional spectrum across the equilibrium saturation ranges of wind-generated surface waves. *Journal of Physical Oceanography*, *47*(8), 2123–2138. https://doi.org/10.1175/JPO-D-17-0017.1

Padhy, C. P., Sen, D., & Bhaskaran, P. K. (2008). Application of wave model for weather routing of ships in the North Indian Ocean. *Natural Hazards*, *44*(3), 373–385. https://doi.org/10.1007/s11069-007-9126-1

Phillips, O. M. (1985). Spectral and statistical properties of the equilibrium range in wind-generated gravity waves. *Journal of Fluid Mechanics*, *156*(1), 505–531. https://doi.org/10.1017/S0022112085002221

Potter, H., Collins, C. O., III, Drennan, W. M., & Graber, H. C. (2015). Observations of wind stress direction during Typhoon Chaba (2010). *Geophysical Research Letters*, *42*(22), 9898–9905. https://doi.org/10.1002/2015GL065173

Powell, M. D., Vickery, P. J., & Reinhold, T. A. (2003). Reduced drag coefficient for high wind speeds in tropical cyclones. *Nature*, *422*(6929), 279–283. https://doi.org/10.1038/nature01481

Raghukumar, K., Chang, G., Spada, F., Jones, C., Janssen, T., & Gans, A. (2019). Performance characteristics of "spotter," a newly developed real-time wave measurement buoy. *Journal of Atmospheric and Oceanic Technology*, *36*(6), 1127–1141. https://doi.org/10.1175/JTECH-D-18-0151.1

Ribal, A., & Young, I. R. (2019). 33 years of globally calibrated wave height and wind speed data based on altimeter observations. *Scientific Data*, *6*(1), 1–15. https://doi.org/10.1038/s41597-019-0083-9

Roemmich, D., Church, J., Gilson, J., Monselesan, D., Sutton, P., & Wijffels, S. (2015). Unabated planetary warming and its ocean structure since 2006. *Nature Climate Change*, *5*(3), 240–245. https://doi.org/10.1038/nclimate2513

Sarmiento, J. L., Hughes, T., Stouffer, R. J., & Manabe, S. (1998). Simulated response of the ocean carbon cycle to anthropogenic climate warming. *Nature*, *393*(6682), 245–249. https://doi.org/10.1038/30455

Shimura, T., Hemer, M., Lenton, A., Chamberlain, M. A., & Monselesan, D. (2020). Impacts of ocean wave-dependent momentum flux on global ocean climate. *Geophysical Research Letters*, *47*(20), e2020GL089296. https://doi.org/10.1029/2020GL089296

Shimura, T., Mori, N., Takemi, T., & Mizuta, R. (2017). Long-term impacts of ocean wave-dependent roughness on global climate systems. *Journal of Geophysical Research: Oceans*, *122*(3), 1995–2011. https://doi.org/10.1002/2016JC012621

Shimura, T., Mori, N., Urano, D., Takemi, T., & Mizuta, R. (2022). Tropical cyclone characteristics represented by the ocean wave-coupled atmospheric global climate model incorporating wave-dependent momentum flux. *Journal of Climate*, *35*(2), 499–515. https://doi.org/10.1175/JCLI-D-21-0362.1

Smit, P. B., Houghton, I. A., Jordanova, K., Portwood, T., Shapiro, E., Clark, D., et al. (2021). Assimilation of significant wave height from distributed ocean wave sensors. *Ocean Modelling*, *159*(December 2020), 101738. https://doi.org/10.1016/j.ocemod.2020.101738

Spencer, M. W., Wu, C., & Long, D. G. (2000). Improved resolution backscatter measurements with the SeaWinds pencil-beam scatterometer. *IEEE Transactions on Geoscience and Remote Sensing*, *38*(1), 89–104. https://doi.org/10.1109/36.823904

Tamura, H. K., Kawaguchi, T., Iwamoto, T., & Fujiki, T. (2021). Coastal destruction and unusual wave spectra induced by Typhoon Faxai in 2019. *Coastal Engineering Journal*, *63*(1), 92–105. https://doi.org/10.1080/21664250.2021.1877944

The Washington Post. (2020). Retrieved from https://www.washingtonpost.com/weather/2020/12/18/ocean-observing-sofar-buoys/

Thomson, J., D'Asaro, E. A., Cronin, M. F., Rogers, W. E., Harcourt, R. R., & Shcherbina, A. (2013). Waves and the equilibrium range at ocean weather station P. *Journal of Geophysical Research: Oceans*, *118*(11), 5951–5962. https://doi.org/10.1002/2013JC008837

Toba, Y. (1973). Local balance in the air-sea boundary processes—II. Partition of wind stress to waves and current. *Journal of the Oceanographical Society of Japan*, *29*(2), 70–75. https://doi.org/10.1007/BF02109506

Voermans, J. J., Smit, P. B., Janssen, T. T., & Babanin, A. V. (2020). Estimating wind speed and direction using wave spectra. *Journal of Geophysical Research: Oceans*, *125*(2), 1–16. https://doi.org/10.1029/2019JC015717